Research Article Vol. 31, No. 4 / 13 Feb 2023 / Optics Express 6782
Optics EXPRESS

Metasurface supporting quasi-BIC for optical trapping and Raman-spectroscopy of biological nanoparticles

MD RABIUL HASAN AND OLAV GAUTE HELLESØ*

Department of Physics and Technology, UiT The Arctic University of Norway, Tromsø, Norway
*olav.gaute.helleso@uit.no

Abstract: Optical trapping combined with Raman spectroscopy have opened new possibilities for analyzing biological nanoparticles. Conventional optical tweezers have proven successful for trapping of a single or a few particles. However, the method is slow and cannot be used for the smallest particles. Thus, it is not adapted to analyze a large number of nanoparticles, which is necessary to get statistically valid data. Here, we propose quasi-bound states in the continuum (quasi-BICs) in a silicon nitride (Si_3N_4) metasurface to trap smaller particles and many simultaneously. The quasi-BIC metasurface contains multiple zones with high field-enhancement ('hotspots') at a wavelength of 785 nm, where a single nanoparticle can be trapped at each hotspot. We numerically investigate the optical trapping of a type of biological nanoparticles, namely extracellular vesicles (EVs), and study how their presence influences the resonance behavior of the quasi-BIC. It is found that perturbation theory and a semi-analytical expression give good estimates for the resonance wavelength and minimum of the potential well, as a function of the particle radius. This wavelength is slightly shifted relative to the resonance of the metasurface without trapped particles. The simulations show that the Q-factor can be increased by using a thin metasurface. The thickness of the layer and the asymmetry of the unit cell can thus be used to get a high Q-factor. Our findings show the tight fabrication tolerances necessary to make the metasurface. If these can be overcome, the proposed metasurface can be used for a lab-on-a-chip for mass-analysis of biological nanoparticles.

1. Introduction

A blood-sample contains a vast number of biological nanoparticles of various types. One example is extracellular vesicles (EVs), which includes exosomes (diameter 30–100 nm) and microvesicles (diameter 100–1000 nm). EVs are considered a mechanism for intercellular communications, allowing cells to exchange proteins, lipids, and genetic material [1–3]. They can be important indicators of different conditions of a producing organism, and therefore can have applications in clinical settings. EVs are heterogeneous and exist in large numbers. Methods that analyse a sample of fluid, i.e., average over all the EVs in the sample, thus have limited usefulness as they do not capture the heterogeneous nature of the EVs and can hide important features present only for a few EVs in a population. Likewise, a method that analyses a limited number of EVs does not give statistically valid information about the population of EVs. By combining optical tweezers with Raman-spectroscopy to do 'Raman tweezers microspectroscopy', the composition of a single, suspended EV can be obtained [4–6]. However, the method is limited to particles that are larger than 100 nm in diameter and particles are analysed one at a time, and it thus takes time to build up statistics. The aim of this work is to investigate methods that can analyse biological nanoparticles one-by-one, but in parallel, with Raman-spectroscopy.

Nanophotonics offers several methods that can trap smaller particles, e.g., slit-waveguides [7,8] and photonic crystals [9–11]. But these methods typically rely on silicon, which is not transparent in the near-visible wavelengths and thus cannot be combined with Raman-spectroscopy. The

#473064 https://doi.org/10.1364/OE.473064
Journal © 2023 Received 16 Aug 2022; revised 13 Jan 2023; accepted 17 Jan 2023; published 9 Feb 2023

Optics EXPRESS

use of plasmonics and surface-enhanced Raman-scattering (SERS) [12–14] is problematic. The spectrum collected from one particle at one location can be different from that collected at another location due to different surface enhancement. In this paper, we propose to use a metasurface consisting of tilted elliptical bars, made of silicon nitrite (Si_3N_4), to trap biological nanoparticles and analyse them with Raman-spectroscopy. Optical trapping using a silicon metasurface with elliptical bars has been proposed at a near-infrared (NIR) wavelength (1550 nm) [15]. Here, the metasurface dimensions are modified so that the operating wavelength can be moved from NIR to a near-visible wavelength, here 785 nm. As opposed to silicon, Si_3N_4 is transparent at 785 nm, making it suitable for combining optical trapping and Raman-spectroscopy. The fabrication technology for Si_3N_4 is mature and it has thus been chosen for the simulations in this work. There are also other suitable materials with comparable or higher refractive index, e.g., Ta_2O_5 and TiO_2. The methods used and the overall results reported in this work will be valid for these materials too, but with the precise values depending on the refractive index.

A metasurface with elliptical bars can support quasi-bound states in the continuum (quasi-BICs) [15–18], which gives large electric field enhancement that we propose to use for trapping and excitation of Raman-scattering. True BICs are nonradiating states of light showing an infinite Q-factor [19], while quasi-BICs have a finite Q-factor. A metasurface with elliptical bars shows a true BIC for a perfectly symmetric structure (parallel elliptical bars), as previously shown in several works [15–18]. Introducing an in-plane asymmetry by rotating the bars results in a quasi-BIC [16], giving a finite Q-factor. Asymmetry can also be achieved by asymmetrically changing the ellipticity of the bars [17]. Even in a perfectly symmetry-protected system, the Q-factor is finite due to the finite size of the structure and material absorption [20]. Additionally, adding a perturbation element to a symmetric structure can also create a quasi-BIC, as demonstrated in [21].

To support a quasi-BIC at 785 nm wavelength, we find that the dimensions of the structure are small. Fabrication of the device will thus be challenging, and we numerically investigate the fabrication tolerances. Particular attention is given to the thickness of the metasurface, as it can influence the Q-factor significantly and it has not been studied previously (to the best of our knowledge). The size of the trapped particle influences the resonance wavelength, and we investigate this shift away from the resonance of the empty metasurface, i.e., without trapped nanoparticles. The influence of trapped nanoparticles on the resonance characteristics has been theoretically investigated in Refs. [15,22]. To reveal the influence on the trapping performance, we find semi-analytical expressions for the trapping potential and the wavelength giving the minimum of the potential well, which are both confirmed by numerical simulations. Whereas this work is based on extensive numerical simulations, it thus shows that limited simulations and semi-analytical expressions are sufficient for future analysis of the structure.

Raman scattering is extremely weak, with only one in 10^6 to 10^{10} photons stimulating vibrational modes [23]. Surface-enhanced Raman spectroscopy (SERS) is typically used to enhance the Raman scattering and enhancement factors of 10^7 to 10^{10} have been achieved, enabling single molecule detection [24]. We show that the high electric field enhancement in the metasurface can give an enhanced Raman scattering at multiple locations. The achievable Raman enhancement factor is generally lower than for SERS, but comparable enhancement values have previously been used for Raman spectroscopy of EVs [25] and single molecule detection [26]. By coupling each location to a channel of a multi-channel spectrometer, Raman-spectra of individual trapped particles can be acquired in parallel.

2. Metasurface design and simulation method

A unit cell of the metasurface investigated is shown in Fig. 1(a), consisting of two identical elliptical bars aligned with a tilt-angle $\pm\theta$. Periodic boundary conditions are used such that the simulated metasurface consists of an infinite array of unit cells. The design parameters of the unit

Optics EXPRESS

cell are also shown in Fig. 1(a), where P_x and P_y are the periodicities along x and y axis, a and b are the long and short axes of the bars, respectively, and h is the height of the bars. The design parameters (P_x, P_y, a, and b) are varied by a scaling factor S, using the relations $P_x \times S$, $P_y \times S$, $a \times S$, and $b \times S$, respectively. The unit cell is covered by water for the purpose of nanoparticle trapping. We use a software based on the finite element method (COMSOL Multiphysics v.5.6) to simulate the unit cell in an infinite array that forms a metasurface. We apply a port with an incident plane wave at the top and a receiving port on the bottom of the substrate. The plane wave is polarized along the x-axis (see Fig. 1(a)). Periodic boundary conditions are set on the faces of the unit cell in the x and y directions. For the simulation of the optical forces, we use an input intensity of 1 mW/μm^2 and integrate the Maxwell stress tensor over the surface of a nanosphere to find the forces. The refractive indices are set to $n_{Si_3N_4} = 2.02$ [27], $n_{SiO_2} = 1.461$ [28], and $n_{water} = 1.33$ [29]. A refractive index of $n_{EV} = 1.39$ [30] is used for the nanosphere to resemble an EV. A user defined mesh with a maximum element size of 12 nm is used for the elliptical bars. For the trapped nanospheres, the maximum element size is set to 3 nm. We use a step size of 0.25 pm for the wavelength sweep to resolve the spectral features.

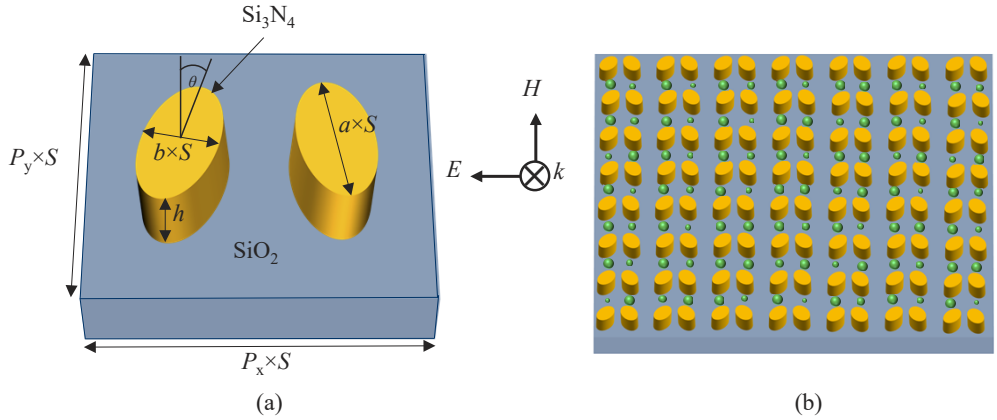

Fig. 1. (a) Schematic of the unit cell of the Si_3N_4 quasi-BIC metasurface with its geometrical parameters. (b) Schematic illustration of trapping of multiple nanospheres (green) using the proposed metasurface.

3. Results and discussion

For this work, the target resonance wavelength λ_0 of the quasi-BIC cavity is 785 nm, which is a wavelength commonly used for Raman-spectroscopy. To achieve this λ_0, we systematically tune the scaling factor and height of the bars (see Supplement 1). The tilt angle for the bar is set to $\theta = \pm 10°$ for all simulations. Figure 2(a) illustrates the reflectance spectrum with $P_x = 522.1$ nm, $P_y = 336.1$ nm, $a = 255.05$ nm, $b = 125.03$ nm, $S = 1$, and $h = 230$ nm, showing a reflectance peak of unity at 785 nm. This corresponds to the resonance wavelength λ_0 of the quasi-BIC mode, without any particle in the unit cell (empty cavity). The symmetry of the proposed metasurface is broken by introducing the tilt angle ($\theta = \pm 10°$), resulting in a finite Q-factor [16]. We fit the reflectance spectra in Fig. 2(a) with a Fano lineshape to extract the Q-factor using a Matlab curve fitting tool. The Fano lineshape formula is given by [15,31]:

$$R = \left| a_1 + ia_2 + \frac{b}{\omega - \omega_0 + i\gamma} \right|^2, \tag{1}$$

where a_1, a_2, and b are the fitting parameters, ω_0 is the central resonance frequency, and γ is the overall damping rate of the resonance. In Eq. (1), normalized ω and ω_0 are used, so that other

Optics EXPRESS

unknown parameters are within 0 to 1. The Q-factor is then computed by using $Q = \omega_0/2\gamma$. It is known that the Q-factor scales with $\sin^{-2}\theta$ [16,32,33] and this is not investigated further in this paper. Also, a thickness $h = 230$ nm is used initially and for the stated field-enhancement. The reflectance spectrum shown in Fig. 2(a) has a narrow linewidth, giving a high Q-factor of 1.3×10^4.

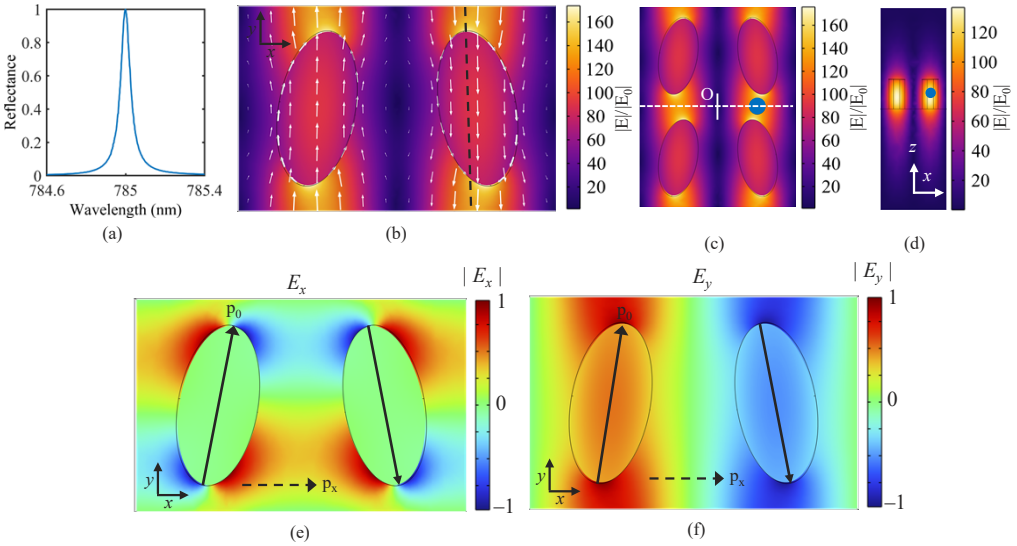

Fig. 2. (a) Simulated reflectance spectra showing $\lambda_0 = 785$ nm. Electric field enhancement profile in the xy plane at $z = 115$ nm (mid-height of the bar) for (b) an empty unit cell and (c) two unit cells with a 50 nm diameter trapped nanosphere. In (b), white arrows indicate the polarization vector of the near fields. The middle of the tip-to-tip gap is indicated with a horizontal dotted-line in (c), and the field enhancement along this line is shown in (d) in the zx plane. The trapped nanosphere is located at $x = P_x/4$, $y = 0$, and $z = 115$ nm, relative to the origin (marked by O in (c)). (e),(f) Electric field patterns with associated dipole moments shown by the black arrows, where p_0 is the dipole moment of a single elliptical bar and p_x is the net dipole moment of the unit cell.

One of the key advantages of BIC metasurfaces is the extreme field localization that results in a large electric field enhancement $|E|/|E_0|$, where $|E|$ is the absolute value of the local electric field with a metasurface and $|E_0|$ is the absolute value of the electric field without the metasurface. To investigate the field enhancement, we first consider an infinite array of empty unit cells, i.e., without trapped particles. The near-fields and the polarization vectors are plotted in Fig. 2(b) at $z = 115$ nm (half the height of the bars). The excited quasi-BIC mode originates from in-plane electric quadrupoles and out-of-plane magnetic dipoles, as also reported in [21,34]. The color bar indicates a maximum field enhancement of 177 on the tips of each elliptical bar. We also simulate a metasurface with two unit cells, including the gap between the bars (along z-axis), where a nanoparticle can be trapped. For the design parameters resulting in λ_0 at 785 nm, the gap size is 81 nm. This imposes an upper limit for the diameter of nanoparticles that can be trapped. In our study, we consider diameters up to 70 nm, which is comparable to small EVs or exosomes [35]. The proposed method will thus be complimentary to 'Raman tweezers microscopy', which is limited to particles larger than 100 nm. The field enhancement with a 50 nm diameter nanosphere in the center of the gap is shown in Fig. 2(c). Interestingly, the introduction of the nanosphere only has limited influence on the maximum field enhancement. This can be explained by the small refractive index difference between the particle ($n_{EV} = 1.39$) and the surrounding water

Optics EXPRESS

($n_{\text{water}} = 1.33$). The field enhancement is maximum on the tips of the bars (Fig. 2(c)), at 177 as previously stated, and decreases to 139 in the middle of the gap (Fig. 2(d)). The enhancement can be increased further by reducing the tilt angle θ [15] or reducing the thickness, as will be discussed below. Note that there are two hotspots per unit cell, and the case of Fig. 2(c) thus corresponds to 25% occupancy for the array. An array of unit cells can trap a large number of particles, possibly with only a single particle trapped at each hotspot (see Fig. 1(b)). A metasurface with quasi-BIC can thus be an efficient way to trap multiple nanoparticles simultaneously.

The high electric field enhancement in the gaps between the tips of the bars can be used to enhance Raman scattering. When a nanoparticle is trapped in the gap, the incident laser light can excite Raman scattering, which extends over a wide range of wavelengths, depending on the chemical composition of the particle. The Raman enhancement factor EF_{Raman} can be quantified by the following expression [36],

$$EF_{\text{Raman}} = \left|\frac{E}{E_0}\right|^2 \times \left|\frac{E_{\text{emission}}}{E_0}\right|^2, \tag{2}$$

where $|E|^2/|E_0|^2$ is the field intensity enhancement at the incident wavelength and $|E_{\text{emission}}|^2/|E_0|^2$ is the field intensity enhancement at the Raman emission wavelength. The Raman scattered light can have a different polarization than that of the incident light. Here, we assume that the polarization of the Raman scattered light is either parallel or perpendicular to the polarization of the incident light. To determine the field enhancement at the Raman emission wavelengths, we take the average field enhancement of the parallel and the perpendicular polarization. This simulation was carried out with a plane wave incident on the metasurface. An alternative approach would be to use a point dipole as an emitter at the equilibrium position in the gap. We have not considered the numerical aperture of any collecting optics. Figure 3(a) shows electric field enhancement for the parallel and perpendicular polarization as a function of Raman emission wavelengths ranging from 790 to 900 nm. The field enhancements for both polarizations are small, resulting in a low average field enhancement around ~ 1.05 over the whole spectrum. Using the maximum field enhancement in the middle of the gap ($|E|/|E_0| = 139$) and inserting the calculated average enhancement into Eq. (2), we find the Raman enhancement factor EF_{Raman}. This gives a significant enhancement of the obtained Raman-signal, with a calculated enhancement of $> 2 \times 10^4$ over the broad emission spectrum, for excitation at the resonance wavelength (Fig. 3(a)). Field enhancement profiles, at a randomly chosen Raman emission wavelength of $\lambda = 820$ nm, are shown in Figs. 3(b),(c) for parallel and perpendicular polarization, respectively. Enhancement at the emission wavelengths, in addition to enhancement at the excitation wavelength, would be an advantage if the enhancement is independent of wavelength. That is a difficult requirement to achieve.

Apart from the high field enhancement, the strong field localization in the gap provides a small mode volume V_{m}. We calculate mode volume V_{m} using the formula [37],

$$V_{\text{m}} = \frac{\iiint \varepsilon(\text{r})|\text{E}(\text{r})|^2 \text{d}^3\text{r}}{\max\left(\varepsilon(\text{r})|\text{E}(\text{r})|^2\right)}, \tag{3}$$

where $\varepsilon(\mathbf{r})$ is the dielectric function and $\mathbf{E}(\mathbf{r})$ is the electric field. The numerator indicates a volume integration performed over the unit cell, while the denominator indicates the maximum over the volume of the unit cell. For the empty cavity with one trapping location, the simulation predicts an extremely small V_{m} of $0.03 \times (\lambda/n_{\text{water}})^3$. The introduction of a nanosphere in the cavity leads to a minor change in the Q-factor and V_{m} (see Supplement 1). The high Q-factor and small V_{m} in this and other proposed metasurfaces may find applications in nonlinear photonics, e.g., for third harmonic generation (THG) [38,39]. As the intensity necessary for THG scales with the factor $(Q/V_{\text{m}})^3$ [40], an enhanced nonlinear response can be achieved.

Optics EXPRESS

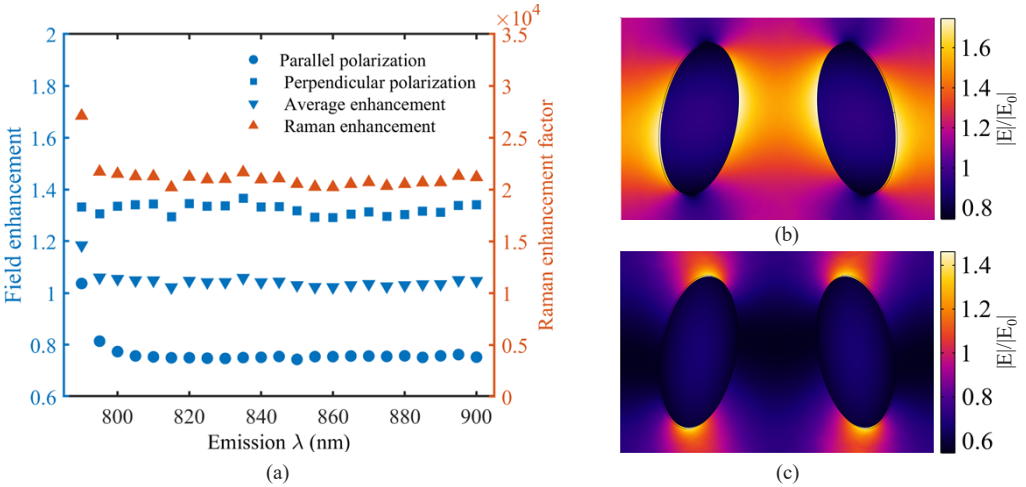

Fig. 3. (a) Field enhancement and Raman enhancement factor EF_{Raman} as a function of Raman emission wavelength. Field enhancement profile for (b) parallel and (c) perpendicular polarization at $\lambda = 820$ nm.

The mathematical definition of mode volume in Eq. (3) is widely used for resonance cavity but not applicable for plasmonic systems as the integrand becomes negative [41]. In addition, calculation of mode volume by this equation is not valid for an open cavity system where fields are not strictly confined [42]. Quasi-normal modes formalism [42,43] and finding local density of optical states with Q-factor [44] are two known approaches that can give an accurate mode volume. In our case, we have studied a dielectric system, which can be roughly treated as a closed cavity system as the fields are tightly confined to finite space with an extremely small leakage. Also, we note that the expression of mode volume in Eq. (3) has been used in other dielectric quasi-BIC systems [22,45].

The dimensions of a fabricated metasurface may deviate from the target dimensions, due to fabrication tolerances and defects. To quantify the impact of such deviations on the Q-factor and the resonance wavelength, we perform numerical simulations as function of the geometrical parameters S and h. The first relationship, between the scaling factor S and the resonance wavelength, is simply that λ_0 is linear with S. The graph in Fig. 4(a) confirms this, with a small difference in slope. Note that the linear relationship and the slope is irrespective of the refractive index of the material. The Q-factor is modestly affected by the change of S, as shown in the same figure. The effect of changing the height h of the bars is shown in Fig. 4(b). The resonance wavelength is approximately linear with h. A variation of h with ± 5% gives ± 3 nm change of the resonance wavelength $\delta\lambda_0$, compared to ± 39 nm for a similar change of S. The sensitivity to h is thus significantly weaker than to the scaling factor S. This can be expected as h influences the resonance through the effective refractive index of the mode, whereas S affects the cavity-dimensions in the plane of the resonance. Finally, the Q-factor shows a higher sensitivity to changes of h, as opposed to the modest sensitivity to changes of S. In particular, the Q-factor increases drastically for small bar heights, for example $h = 40$ nm. To further investigate the dependence of the Q-factor on h, we fit the line $Q = a/(h–h_0)^2 + Q_0$ (dashed line in Fig. 4(b)). The values fitted to a, h_0 and Q_0 are 4.4×10^8 nm^2, 18 nm and 2460, respectively. This is consistent with previous works, which have shown that the Q-factor generally varies with the inverse square of the asymmetry factor, as α^{-2} [16,39]. As the height h approaches h_0, the mode stretches further into the substrate and is less affected by the asymmetry of the bars, giving an increase of the Q-factor and field enhancement. This is illustrated in Fig. 5, which shows electric

Optics EXPRESS

field distributions of the quasi-BIC for different bar heights. At $h = 230$ nm, the mode is mostly confined in water with a small part stretching into the underlying substrate. As the height is reduced, the mode extends further into the substrate region, as is clear for $h = 60$ nm. There are thus two factors that influence the Q-factor of our structure, namely the angle θ of the bars and their height h. To reach a high Q-factor for a fabricated structure, it can be advantageous to use a small h-value and a somewhat larger θ, as the thickness of a deposited layer can generally be tightly controlled, whereas a small angle θ can be masked by defects and topography changes during fabrication. We thus propose a thin metasurface as an alternative to small asymmetry in the xy-plane. As thickness is reduced, the dependency of the Q-factor on the thickness becomes more prominent, and generally the structure will be more prone to fabrication errors as the thickness is reduced.

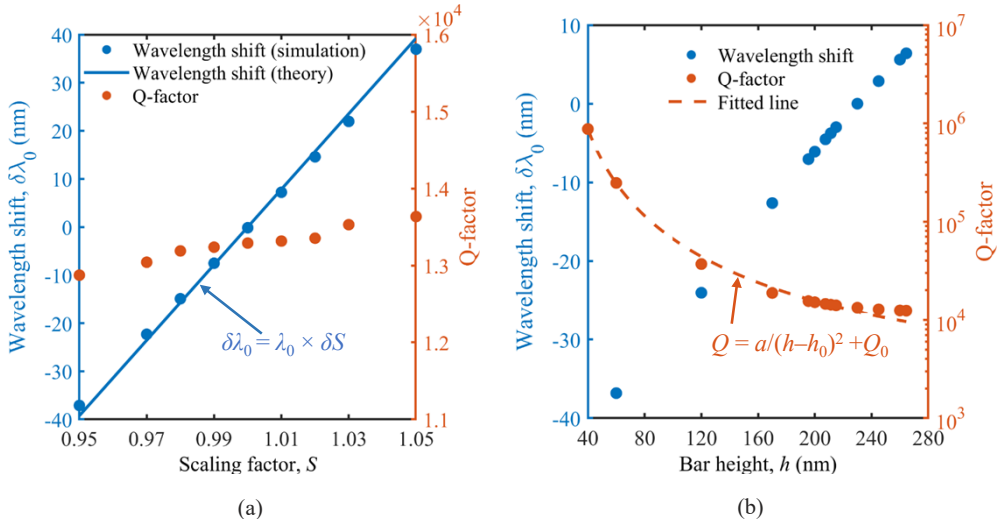

Fig. 4. Wavelength shift and Q-factor for deviations in (a) scaling factor S and (b) height h from the dimensions giving $\lambda_0 = 785$ nm ($S = 1$ and $h = 230$ nm). The straight blue line in (a) shows the linear prediction for S, while the dashed orange line in (b) is fitted to the Q-factors. An infinite array of the single unit cell is simulated for both (a) and (b).

In this work, we consider an ideal scenario by assuming an infinite array of perfect unit cells in a lossless material. For a fabricated metasurface with finite size, the resonance wavelength of the quasi-BIC may shift towards a shorter or longer wavelength [15]. In addition, the reflectance spectrum for a finite size metasurface is expected to be broadened, resulting in a reduced Q-factor [46]. The Q-factor of the quasi-BIC also depends on structural imperfections and material losses [20], and the Q-factor of a fabricated metasurface may thus have a different dependence on size than for a simulated array. Experimentally, the finite size of the metasurface will not significantly influence the Q-factor, and it will most likely be dominated by fabrication errors.

Before studying the forces on a trapped particle, we investigate the reflectance spectrum and how a quasi-BIC mode is influenced by a trapped nanosphere. The optimized dimensions found earlier were used, giving $\lambda_0 = 785$ nm for the empty cavity. We start by finding the shift in resonance wavelength $\delta\lambda_c$ when a nanosphere is introduced into the cavity (25% occupancy). A generalized approach to find $\delta\lambda_c$ is to apply cavity perturbation theory, which supposes a slight modification of the electromagnetic field inside the cavity due to the introduction of an external object. As a result, the resonant mode changes slightly, inducing a frequency shift $\delta\omega_c$ [47], that

Optics EXPRESS

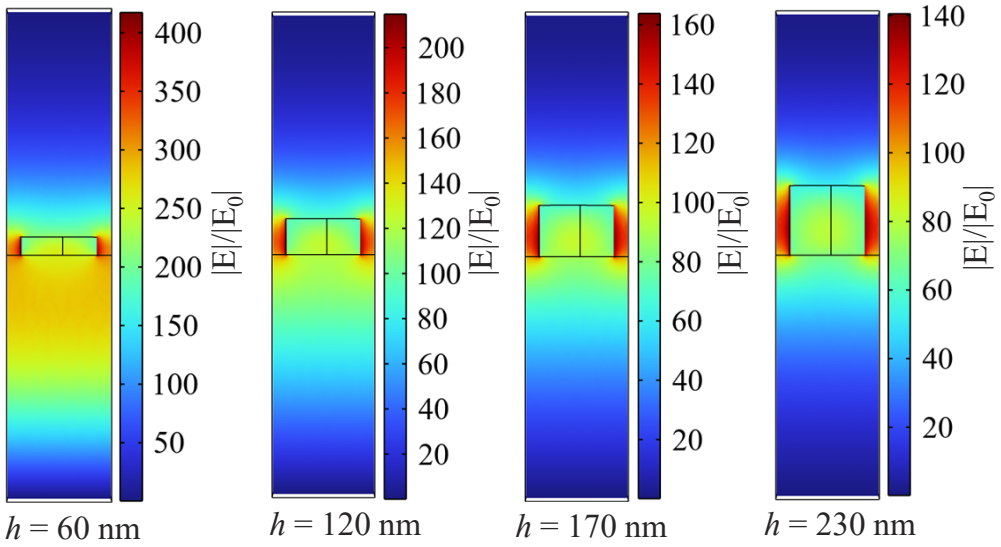

Fig. 5. Electric field distribution of the quasi-BIC for different bar heights. The fields are normalized to the incident electric field. An infinite array of single unit cells is simulated. The field distribution is taken along the yz plane with $x = P_x/4$ (see the black dashed line Fig. 2(b)).

can be expressed in terms of $\delta\lambda_c$ by:

$$\delta\lambda_c = \frac{\lambda_0}{2} \frac{\iiint d^3\mathbf{r}\, \Delta\varepsilon(\mathbf{r})|\mathbf{E}(\mathbf{r})|^2}{\iiint d^3\mathbf{r}\, \varepsilon(\mathbf{r})|\mathbf{E}(\mathbf{r})|^2}, \tag{4}$$

where λ_0 is the resonance wavelength of the unperturbed cavity, $\mathbf{E}(\mathbf{r})$ is the electric field of the unperturbed mode, $\varepsilon(\mathbf{r})$ is the dielectric function, and $\Delta\varepsilon(\mathbf{r})$ is the change of dielectric function due to the external object. Using Eq. (4), $\delta\lambda_c$ is calculated numerically and plotted in Fig. 6(a) (blue dashed line) as function of nanosphere radius. As expected, bigger nanospheres induce larger shifts $\delta\lambda_c$, with a $\delta\lambda_c$ of 132 pm for a nanosphere radius of 35 nm. To verify this result based on perturbation theory, we perform simulations of two unit cells with a trapped nanosphere positioned at the gap center and as function of wavelength. The nanosphere causes the reflectance peak to shift. Reflectance spectra for different radii of the nanosphere is shown in Fig. 6(b). Increasing the nanosphere radius results in a red shift, i.e., reflectance peak shifts towards a longer wavelength compared to the empty cavity wavelength of 785 nm. The $\delta\lambda_c$ calculated from the reflectance peak are plotted in Fig. 6(a) (filled triangles) together with the results of the perturbation theory. The close correspondence shows that the perturbation theory gives a good approximation for the wavelength shift of the peak in reflectivity. For an infinite array of identical unit cells, the integration in Eq. (4) is carried out over a unit cell, as was done here. However, Eq. (4) is also valid if integrating over the entire array. A small perturbation $\Delta\varepsilon(\mathbf{r})$, e.g., one trapped nanosphere in a large array, will thus give an insignificant change in the resonance wavelength. As the number of trapped particles increase, a linear increase of wavelength shift is expected with the number of trapped particles, as $\Delta\varepsilon(\mathbf{r})$ increases linearly. We verify this for two trapped nanospheres (50% filling of the array). In this case, $\delta\lambda_c$ increases by a factor 2.

The simulations reported here consider the ideal case of identical unit cells and identical particles. For an array with variations in the size of the unit cell, either intended or due to fabrication errors, and for variations in the size of the trapped particles, further simulations and development of the theory is necessary to give a quantitative description. However, a qualitative

Optics EXPRESS

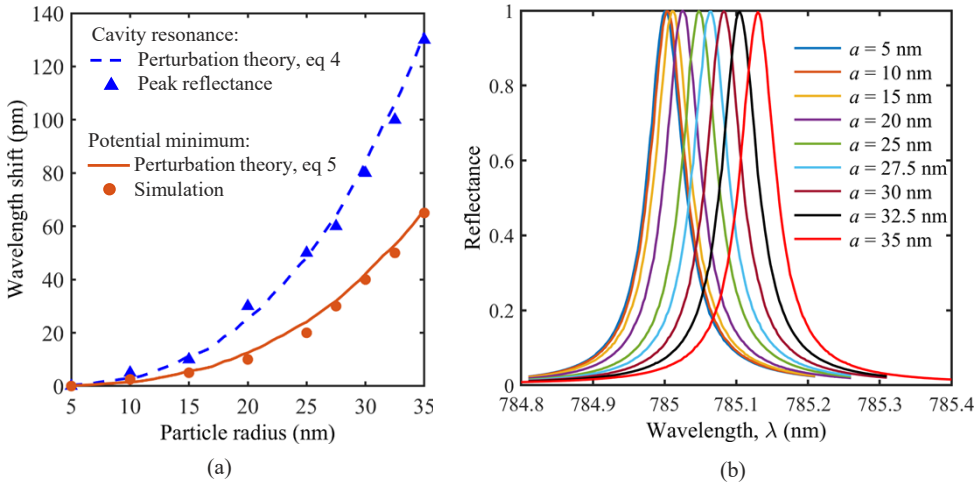

Fig. 6. (a) Resonance wavelength shift $\delta\lambda_c$ from perturbation theory (blue dashed line) and from numerical simulation for peak reflectance (blue triangles), and shift $\delta\lambda_L$ giving the minimum trapping potential, from Eq. (5) (orange solid line) and from numerical simulation (orange circles), all as function of nanosphere radius. (b) Reflectance spectra for different radii of the trapping nanosphere. The nanosphere is placed at $x = P_x/4$, $y = 0$, and $z = 100$ nm. For this study, an infinite array of two unit cells is simulated.

description of the influence on the reflection spectrum can be given. Both variations in the size of the unit cell and in the size of the particles will result in a reduction of the Q-factor related to the standard deviations of the distributions. There can also be a shift in the resonance wavelength related to the mean size of the unit cell and the mean size of the particles. In principle, it is thus possible to determine the size-distribution of the particles from the change in Q-factor and the resonance shift between an empty metasurface and a metasurface with particles. Note that the Q-factor and the wavelength shift also depend on the occupancy rate, and the relationship is thus complicated.

As discussed earlier, the metasurface shows localized near-field hotspots in the gaps between the bars. Due to the gradient of the localized field intensity, an optical gradient force is produced. This force attracts the trapping particles towards the middle of the gaps, while Brownian motion and unintended scattering from imperfect structures, will tend to push the trapped particles out of the trap. To study optical trapping, we again consider a two-unit cell that shares one trapped nanosphere in the middle of the gap. The two-unit cell is repeated, meaning that the trapped nanospheres are also repeated and located exactly at the same position in the gap in the infinite array. This is clearly not a realistic situation, and we will return to the case of one or few particles. The case of many particles at random positions in the gap will not be treated statistically.

To find the conditions for stable trapping of nanoparticles, we investigate the trapping potential and how it is influenced by the size of the trapped particle and the wavelength. The trapping potential U is a function of the wavelength, as was found for the reflectance, and this function is influenced by the radius of the nanosphere. We use numerical simulation of the field-distribution and the Maxwell stress tensor to find this dependency for the optimized metasurface ($S = 1$ and $h = 230$ nm). The optical force along the vertical axis F_z is found as function of z-position of the trapped nanosphere (see Supplement 1). The force F_z is then integrated along the vertical path from the equilibrium height in the gap ($F_z = 0$ for $z = 100$ nm) up to a position where F_z again approaches zero. This gives the potential U for a certain wavelength and nanosphere radius (see Supplement 1), as shown in Fig. 7(a). The potential for a given radius has a minimum for a

Optics EXPRESS

wavelength that is shifted $\delta\lambda_L$ from the resonance wavelength of the empty cavity. The shifts $\delta\lambda_L$ corresponding to the minima in Fig. 7(a) are plotted in Fig. 6(a) (orange circles). The relationship between this shift $\delta\lambda_L$ for the trapping potential and the shift in the resonance wavelength $\delta\lambda_L$ due to a trapped particle, is simply given by (see Supplement 1):

$$\delta\lambda_L = \delta\lambda_c/2, \tag{5}$$

where $\delta\lambda_c$ is found from perturbation theory, Eq. (4). The trapping potential is most influenced by the wavelength when the force on the particle is maximum. As the force is a gradient force, it is maximum when the field-gradient is maximum, which occurs when the nanosphere is, in qualitative terms, approximately half the way out of the well. Thus, this gives a simple explanation of Eq. (5) as the trapping potential is mostly influenced with the particle at the edge of the well, whereas the reflectance was calculated with the particle at the center of the well.

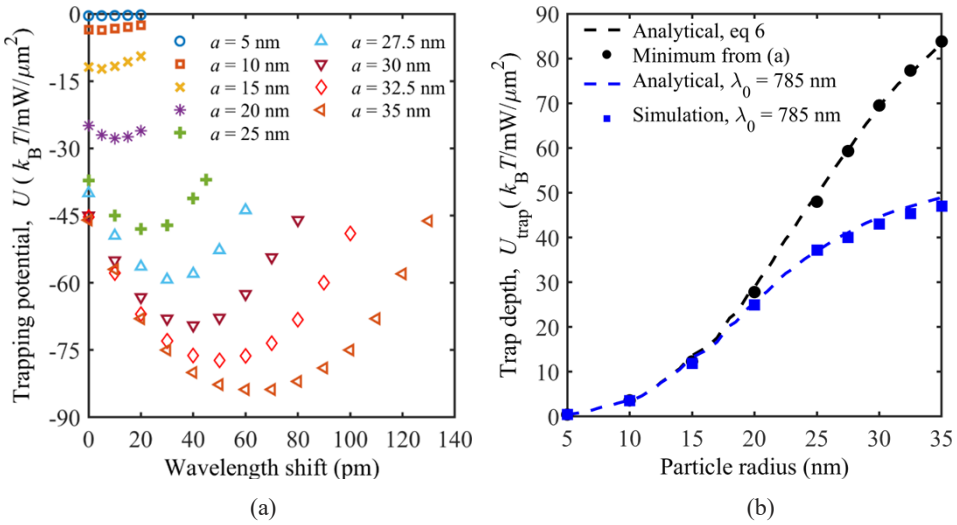

Fig. 7. (a) Trapping potential U as a function of wavelength shift away from the resonance of the empty cavity. (b) Maximum trapping potential depth U_{trap} from the semi-analytical expression (black dashed line) and as the minimum of the graphs in (a) (filled circles). Analytical trap depth (blue dashed line) is compared with simulated values (filled squares) for the empty cavity resonance wavelength of 785 nm.

The wavelength shift given by Eq. (5) is also plotted in Fig. 6(a) (orange solid line). The correspondence between this semi-analytical result and the numerical simulation is good. The numerical simulation involves finding the field-distribution at a number of positions as the nanosphere is moved out of the potential, and as function of wavelength. It is thus a computationally costly procedure. On the other hand, the semi-analytical expression only involves finding the field-distribution with the nanosphere at a single position (in the center of the well and the gap). It is thus significantly faster to perform.

Going one step further, we study in more detail the optical trapping potential and particularly the minima of the curves in Fig. 7(a), which gives the maximum trapping potential depth U_{trap} as function of nanosphere radius. An analytical expression for U_{trap} can be derived from [22] and is given by (see Supplement 1):

$$U_{trap} = 2\hbar N_p \frac{\kappa_{ex}}{\kappa}(\arctan[-\Delta] + \arctan[\eta + \Delta]), \tag{6}$$

where Δ is the (negative) dimensionless detuning between the laser and empty cavity frequencies, η is the dimensionless back-action parameter, and N_p is the number of photons injected into the

Optics EXPRESS

cavity for the input intensity. The mathematical definition of these parameters and details of other parameters in Eq. (6) can be found in Supplement 1.

Using the analytical expression in Eq. (6), U_{trap} is plotted versus nanosphere radius, as shown by the dashed line in Fig. 7(b). The potential U_{trap} increases with nanosphere radius, reaching a value of 84 $k_{\text{B}}T$/mW/μm^2 for a nanosphere radius of 35 nm. The relationship to radius is expected because the polarizability, and thus also the potential, is proportional to nanosphere volume [48]. The trapping time in a trap depends strongly on the trapping potential and the size of the trapped nanosphere [49]. A potential depth of 10 $k_{\text{B}}T$ is generally considered sufficient for stable trapping [50]. We find that a somewhat deeper potential is necessary for the particles considered here, with 11 $k_{\text{B}}T$ giving a trapping time of 10 seconds for a nanosphere with 15 nm radius (see Supplement 1). This is comparable to the integration times used for optical tweezers and Raman-spectroscopy [4]. To obtain this potential depth of 11 $k_{\text{B}}T$, a relatively modest intensity of 1 mW/μm^2 is sufficient, and this intensity can thus be used to trap nanospheres with a radius of 15 nm or larger. Note that this is valid for a filling factor of 25%, with symmetric trapping of the nanospheres, and for a laser wavelength tuned to the resonance for this case. To verify the values of U_{trap} found from Eq. (6), we also find it from the simulations using the Maxwell stress tensor. This is simply taking the minima of the curves in Fig. 7(a) and converting them to potential depth relative to the zero potential. The graph with the semi-analytical results from Eq. (6) and from the fully numerical simulation is shown in Fig. 7(b), with dashed line and filled circles, respectively. Again, the results indicate a good agreement between the two approaches. For the metasurface studied in this work, it is thus sufficient to use the expression in Eq. (6) to fully characterize the trapping potential of the structure. The expression is semi-analytical as it depends on the wavelength shift $\delta\lambda_{\text{L}}$ that gives maximum potential depth, which in turn is found from perturbation theory, Eqs. (4), and (5).

For one or a few trapped particles, the resonance wavelength of an infinite (or large) array does not change, following Eq. (4), as pointed out previously. By consequence, $\lambda_{\text{L}} = \lambda_{\text{c}} = \lambda_0$ and $\Delta = 0$ in Eq. (6). For many particles trapped and a laser wavelength set to the resonance of the empty cavity, we again have $\lambda_{\text{L}} = \lambda_0$ and $\Delta = 0$. Thus, we find that for the laser wavelength set to the resonance of the empty cavity, the potential is independent of the number of trapped particles. This potential is also shown in Fig. 7(b). It is almost identical to the potential for periodic trapping with 25% filling for radii up to 20 nm, while for larger radii it is significantly lower. This implies that the conclusion in the previous paragraph, that an intensity of 1 mW/μm^2 is sufficient to trap nanospheres with a radius of 15 nm or larger, is valid for any number of trapped particles.

4. Conclusion

To conclude, we have proposed a new platform for optical trapping and Raman spectroscopy of multiple nanoparticles using a Si_3N_4 metasurface supporting quasi-BIC. The metasurface consists of an infinite array of unit cells where the unit cell consists of two identical Si_3N_4 elliptical bars deposited on a SiO_2 substrate. We have optimized the design parameters of the unit cell to obtain resonance at a wavelength of 785 nm and investigated how sensitive the resonance wavelength is to changes in these parameters. The sensitivity is high, particularly to the scaling factor S, implying that it will be challenging to fabricate a metasurface with resonance close to 785 nm. We find that the Q-factor increases significantly when the thickness of the metasurface is reduced. To achieve a high Q-factor, the thickness should thus be optimized, in addition to the asymmetry and geometry of the unit cell. We have shown a very high electric field enhancement in the gap center, allowing a means for nanoparticle trapping in the gap. The array of unit cells, with two trapping locations per unit cell, makes it possible to trap many nanoparticles simultaneously using a low input intensity. We have investigated the interplay between the quasi-BIC cavity and trapped nanoparticles, resulting in a shift in resonance wavelength, and we

Optics EXPRESS

have shown how this affects the trapping process. We have used biological nanoparticles, with a refractive index corresponding to small extracellular vesicles, in the simulations. Semi-analytical expressions for wavelength shift and maximum potential depth have been shown to agree well with the simulations, both for many and few trapped particles, and extensive simulations can thus be avoided in future work. We find that a relatively modest power can be used for trapping nanoparticles with diameters of 30–70 nm using near-visible light. The potential depth depends on the wavelength, the radius and the number of particles trapped. Experimentally, a tunable laser must be used, and the wavelength tuned to the peak in reflectance before trapping starts. With few particles trapped, the laser can remain at this wavelength. If the occupancy rate increases significantly, e.g., approaching 25%, it can be adjusted according to Eq. (5) and Fig. 7 to get a deeper potential well. Overall, the results are promising for using a metasurface with quasi-BIC as an on-chip platform for optical trapping of biological nanoparticles. A sufficient signal-to-noise ratio is necessary to combine optical trapping with Raman spectroscopy. The Raman signal increases with the acquisition time. A background signal can be expected due to Raman scattering by the metasurface, and this will also increase with the acquisition time. Consequently, the feasibility of combining trapping and Raman-spectroscopy using quasi-BIC depends partly on the Raman-background of the metasurface. This has not been considered here and will be explored in future experimental work.

Funding. Norges Forskningsråd (302333).

Acknowledgments. The publication charges for this article have been funded by a grant from the publication fund of UiT The Arctic University of Norway.

Disclosures. The authors declare no conflicts of interest.

Data availability. Data underlying the results presented in this paper are available in Ref. [51].

Supplemental document. See Supplement 1 for supporting content.

References

1. J. M. Pitt, G. Kroemer, and L. Zitvogel, "Extracellular vesicles: masters of intercellular communication and potential clinical interventions," J. Clin. Investig. **126**(4), 1139–1143 (2016).
2. G. Raposo and P. D. Stahl, "Extracellular vesicles: a new communication paradigm?" Nat. Rev. Mol. Cell. Biol. **20**(9), 509–510 (2019).
3. M. Yanez-Mo, P. R. Siljander, and Z. Andreu, *et al.*, "Biological properties of extracellular vesicles and their physiological functions," J. Extracell. Vesicles **4**(1), 27066 (2015).
4. S. G. Kruglik, F. Royo, J. M. Guigner, L. Palomo, O. Seksek, P. Y. Turpin, I. Tatischeff, and J. M. Falcon-Perez, "Raman tweezers microspectroscopy of circa 100 nm extracellular vesicles," Nanoscale **11**(4), 1661–1679 (2019).
5. W. Lee, A. Nanou, L. Rikkert, F. A. W. Coumans, C. Otto, L. Terstappen, and H. L. Offerhaus, "Label-Free Prostate Cancer Detection by Characterization of Extracellular Vesicles Using Raman Spectroscopy," Anal. Chem. **90**(19), 11290–11296 (2018).
6. I. Tatischeff, E. Larquet, J. M. Falcon-Perez, P. Y. Turpin, and S. G. Kruglik, "Fast characterisation of cell-derived extracellular vesicles by nanoparticles tracking analysis, cryo-electron microscopy, and Raman tweezers microspectroscopy," J. Extracell. Vesicles **1**(1), 19179 (2012).
7. A. H. Yang, S. D. Moore, B. S. Schmidt, M. Klug, M. Lipson, and D. Erickson, "Optical manipulation of nanoparticles and biomolecules in sub-wavelength slot waveguides," Nature **457**(7225), 71–75 (2009).
8. A. H. Yang, T. Lerdsuchatawanich, and D. Erickson, "Forces and transport velocities for a particle in a slot waveguide," Nano Lett. **9**(3), 1182–1188 (2009).
9. S. Mandal, X. Serey, and D. Erickson, "Nanomanipulation using silicon photonic crystal resonators," Nano Lett. **10**(1), 99–104 (2010).
10. T. van Leest and J. Caro, "Cavity-enhanced optical trapping of bacteria using a silicon photonic crystal," Lab Chip **13**(22), 4358–4365 (2013).
11. C. Renaut, J. Dellinger, B. Cluzel, T. Honegger, D. Peyrade, E. Picard, F. de Fornel, and E. Hadji, "Assembly of microparticles by optical trapping with a photonic crystal nanocavity," Appl. Phys. Lett. **100**(10), 101103 (2012).
12. J. M. Nam, J. W. Oh, H. Lee, and Y. D. Suh, "Plasmonic Nanogap-Enhanced Raman Scattering with Nanoparticles," Acc. Chem. Res **49**(12), 2746–2755 (2016).
13. H. Y. Wu, C. J. Choi, and B. T. Cunningham, "Plasmonic nanogap-enhanced Raman scattering using a resonant nanodome array," Small **8**(18), 2878–2885 (2012).
14. C. Zhan, X. J. Chen, Y. F. Huang, D. Y. Wu, and Z. Q. Tian, "Plasmon-Mediated Chemical Reactions on Nanostructures Unveiled by Surface-Enhanced Raman Spectroscopy," Acc. Chem. Res. **52**(10), 2784–2792 (2019).

Optics EXPRESS

15. S. Yang, C. Hong, Y. Jiang, and J. C. Ndukaife, "Nanoparticle Trapping in a Quasi-BIC System," ACS Photonics **8**(7), 1961–1971 (2021).
16. K. Koshelev, S. Lepeshov, M. Liu, A. Bogdanov, and Y. Kivshar, "Asymmetric Metasurfaces with High-Q Resonances Governed by Bound States in the Continuum," Phys. Rev. Lett. **121**(19), 193903 (2018).
17. Y. Jahani, E. R. Arvelo, F. Yesilkoy, K. Koshelev, C. Cianciaruso, M. De Palma, Y. Kivshar, and H. Altug, "Imaging-based spectrometer-less optofluidic biosensors based on dielectric metasurfaces for detecting extracellular vesicles," Nat. Commun. **12**, 3246 (2021).
18. F. Yesilkoy, E. R. Arvelo, Y. Jahani, M. K. Liu, A. Tittl, V. Cevher, Y. Kivshar, and H. Altug, "Ultrasensitive hyperspectral imaging and biodetection enabled by dielectric metasurfaces," Nat. Photonics **13**(6), 390–396 (2019).
19. C. W. Hsu, B. Zhen, A. D. Stone, J. D. Joannopoulos, and M. Soljačić, "Bound states in the continuum," Nat. Rev. Mater. **1**(9), 16048 (2016).
20. K. Koshelev, G. Favraud, A. Bogdanov, Y. Kivshar, and A. Fratalocchi, "Nonradiating photonics with resonant dielectric nanostructures," Nanophotonics **8**(5), 725–745 (2019).
21. G. Q. Moretti, A. Tittl, E. Cortés, S. A. Maier, A. V. Bragas, and G. Grinblat, "Introducing a Symmetry-Breaking Coupler into a Dielectric Metasurface Enables Robust High-Q Quasi-BICs," Adv. Photonics Res. **3**(12), 2200111 (2022).
22. L. Neumeier, R. Quidant, and D. E. Chang, "Self-induced back-action optical trapping in nanophotonic systems," New J. Phys. **17**(12), 123008 (2015).
23. C. F. Kenworthy, L. Pjotr Stoevelaar, A. J. Alexander, and G. Gerini, "Using the near field optical trapping effect of a dielectric metasurface to improve SERS enhancement for virus detection," Sci. Rep. **11**(1), 6873 (2021).
24. E. C. Le Ru, E. Blackie, M. Meyer, and P. G. Etchegoin, "Surface enhanced Raman scattering enhancement factors: a comprehensive study," J. Phys. Chem. C **111**(37), 13794–13803 (2007).
25. S. L. Dong, Y. H. Wang, Z. Q. Liu, W. W. Zhang, K. Z. Yi, X. G. Zhang, X. L. Zhang, C. Z. Jiang, S. K. Yang, F. B. Wang, and X. H. Xiao, "Beehive-Inspired Macroporous SERS Probe for Cancer Detection through Capturing and Analyzing Exosomes in Plasma," ACS Appl. Mater. Interfaces **12**(4), 5136–5146 (2020).
26. J. Cambiasso, M. Konig, E. Cortes, S. Schlucker, and S. A. Maier, "Surface-Enhanced Spectroscopies of a Molecular Monolayer in an All-Dielectric Nanoantenna," ACS Photonics **5**(4), 1546–1557 (2018).
27. K. Luke, Y. Okawachi, M. R. E. Lamont, A. L. Gaeta, and M. Lipson, "Broadband mid-infrared frequency comb generation in a Si_3N_4 microresonator," Opt. Lett. **40**(21), 4823–4826 (2015).
28. L. V. Rodríguez-de Marcos, J. I. Larruquert, J. A. Méndez, and J. A. Aznárez, "Self-consistent optical constants of SiO_2 and Ta_2O_5 films," Opt. Mater. Express **6**(11), 3622–3637 (2016).
29. M. Daimon and A. Masumura, "Measurement of the refractive index of distilled water from the near-infrared region to the ultraviolet region," Appl. Opt. **46**(18), 3811–3820 (2007).
30. C. Gardiner, M. Shaw, P. Hole, J. Smith, D. Tannetta, C. W. Redman, and I. L. Sargent, "Measurement of refractive index by nanoparticle tracking analysis reveals heterogeneity in extracellular vesicles," J. Extracell. Vesicles **3**(1), 25361 (2014).
31. S. Li, C. Zhou, T. Liu, and S. Xiao, "Symmetry-protected bound states in the continuum supported by all-dielectric metasurfaces," Phys. Rev. A **100**(6), 063803 (2019).
32. Z. Liu, Y. Xu, Y. Lin, J. Xiang, T. Feng, Q. Cao, J. Li, S. Lan, and J. Liu, "High-Q Quasibound States in the Continuum for Nonlinear Metasurfaces," Phys. Rev. Lett. **123**(25), 253901 (2019).
33. M. V. Rybin, K. L. Koshelev, Z. F. Sadrieva, K. B. Samusev, A. A. Bogdanov, M. F. Limonov, and Y. S. Kivshar, "High-Q Supercavity Modes in Subwavelength Dielectric Resonators," Phys. Rev. Lett. **119**(24), 243901 (2017).
34. M. K. Liu and D. Y. Choi, "Extreme Huygens' Metasurfaces Based on Quasi-Bound States in the Continuum," Nano Lett. **18**(12), 8062–8069 (2018).
35. L. M. Doyle and M. Z. Wang, "Overview of Extracellular Vesicles, Their Origin, Composition, Purpose, and Methods for Exosome Isolation and Analysis," Cells **8**(7), 727 (2019).
36. P. Alonso-Gonzalez, P. Albella, M. Schnell, J. Chen, F. Huth, A. Garcia-Etxarri, F. Casanova, F. Golmar, L. Arzubiaga, L. E. Hueso, J. Aizpurua, and R. Hillenbrand, "Resolving the electromagnetic mechanism of surface-enhanced light scattering at single hot spots," Nat. Commun. **3**, 684 (2012).
37. S. Hu and S. M. Weiss, "Design of Photonic Crystal Cavities for Extreme Light Concentration," ACS Photonics **3**(9), 1647–1653 (2016).
38. L. Carletti, S. S. Kruk, A. A. Bogdanov, C. De Angelis, and Y. Kivshar, "High-harmonic generation at the nanoscale boosted by bound states in the continuum," Phys. Rev. Res. **1**(2), 023016 (2019).
39. K. Koshelev, Y. T. Tang, K. F. Li, D. Y. Choi, G. X. Li, and Y. Kivshart, "Nonlinear Metasurfaces Governed by Bound States in the Continuum," ACS Photonics **6**(7), 1639–1644 (2019).
40. M. Notomi, "Strong Light Confinement With Periodicity," Proc. IEEE **99**(10), 1768–1779 (2011).
41. A. F. Koenderink, "On the use of Purcell factors for plasmon antennas," Opt. Lett. **35**(24), 4208–4210 (2010).
42. P. Lalanne, W. Yan, K. Vynck, C. Sauvan, and J. P. Hugonin, "Light Interaction with Photonic and Plasmonic Resonances," Laser Photonics Rev. **12**(5), 1700113 (2018).
43. C. Tao, J. D. Zhu, Y. Zhong, and H. T. Liu, "Coupling theory of quasinormal modes for lossy and dispersive plasmonic nanoresonators," Phys. Rev. B **102**(4), 045430 (2020).
44. I. M. Palstra, H. M. Doeleman, and A. F. Koenderink, "Hybrid cavity-antenna systems for quantum optics outside the cryostat?" Nanophotonics **8**(9), 1513–1531 (2019).

Optics EXPRESS

45. W. Wang and X. D. Ma, "Achieving extreme light confinement in low-index dielectric resonators through quasi-bound states in the continuum," Opt. Lett. **46**(24), 6087–6090 (2021).
46. C. Z. Fang, Q. Y. Yang, Q. C. Yuan, X. T. Gan, J. L. Zhao, Y. Shao, Y. Liu, G. Q. Han, and Y. Hao, "High-Q resonances governed by the quasi-bound states in the continuum in all-dielectric metasurfaces," Opto-Electron. Adv. **4**(6), 200030 (2021).
47. J. D. J. Joannopoulos, G. Steven, Joshua N. Winn, and Robert D. Meade, *Photonic Crystals: Molding the Flow of Light (Second Edition)* (Princeton University Press, 2008).
48. P. Zemanek, A. Jonas, L. Sramek, and M. Liska, "Optical trapping of Rayleigh particles using a Gaussian standing wave," Opt. Commun. **151**(4-6), 273–285 (1998).
49. C. Hosokawa, H. Yoshikawa, and H. Masuhara, "Cluster formation of nanoparticles in an optical trap studied by fluorescence correlation spectroscopy," Phys. Rev. E: Stat., Nonlinear, Soft Matter Phys. **72**(2), 021408 (2005).
50. A. Ashkin, J. M. Dziedzic, J. E. Bjorkholm, and S. Chu, "Observation of a single-beam gradient force optical trap for dielectric particles," Opt. Lett. **11**(5), 288–290 (1986).
51. M. R. Hasan and O. G. Hellesø, "Replication data for : Metasurface supporting quasi-BIC for optical trapping and Raman-spectroscopy of biological nanoparticles," DataverseNO, V1 (2023), https://doi.org/10.18710/VW1M5L.